Focussed on Fracture and Damage Detection in Masonry Structures

Visual Abstract

Comparison of Two Parameters Models for clay brick masonry confined by FRP

Giancarlo Ramaglia, Gian Piero Lignola, Andrea Prota
University of Naples, Federico II, Department of Structures for Engineering and Architecture, Via Claudio 21, Naples, 80125, Italy
giancarlo.ramaglia@unina.it, glignola@unina.it, aprota@unina.it

ABSTRACT. Masonry elements are often confined in order to improve their structural capacity. Generalized methods to assess the behavior of confined masonry columns are usually derived from concrete confinement models. However, concrete and masonry present several crucial differences due to their physical and mechanical properties. The recent scientific researches provided relevant information on the experimental behavior of confined masonry columns. In this paper, the Stassi D'Alia failure criterion, recently particularized by the authors to assess the axial capacity of confined solid clay brick masonry, has been discussed remarking its potential as a solid mechanics model. The model has been validated by means of comparisons with 67 relevant experimental results available in the scientific literature. The tested specimens made of solid clay bricks were strengthened with several types of strengthening systems. In order to assess the potential of the confined model, the comparison included also other four available mechanical models based on classical failure criteria available in the scientific literature. The reliability of the confinement models was remarked by assessing some relevant statistical parameters.

KEYWORDS. Mechanical approach; Masonry; Confinement; Experimental tests.

OPEN ACCESS

Citation: Ramaglia, G., Lignola, G.P., Prota, A., Comparison of Two Parameters Models for clay brick masonry confined by FRP, Frattura ed Integrità Strutturale, 51 (2020) 288-312.

Received: 14.06.2019
Accepted: 26.11.2019
Published: 01.01.2020

INTRODUCTION

Modern strengthening strategies can be performed to improve the structural capacity of several types of structures [1, 2]. For masonry buildings strengthening strategies can be applied to improve different aspects [3, 4]. In particular, intervention strategies can be used to improve both the load capacity [5, 6] and the ductility capacity [7]. Many innovative materials were used in strengthening applications of real structures and heritage buildings since many years [8]. The effectiveness of these systems was demonstrated in many research programs by means of static [9, 10] and dynamic [11, 12] tests. The benefits due to the confinement effects represent a key aspect in the engineering applications. Confinement can be applied by means of wraps made of composite materials [13, 14]. This strengthening

strategy limits or prevents the lateral deformations and increases the axial capacity of the structural member. The increasing of the lateral compression in axially loaded elements provides a three-dimensional stress state. This stress state is beneficial to increase the load capacity of the confined structural member as demonstrated by the classical failure criteria of building materials [15, 16]. In the practical applications, the confinement is used either to confine individual structural elements or entire buildings, or parts of them. The attention focuses on masonry columns where confinement methods accounting for masonry peculiarities are not available in the technical literature. Several models can be used to assess the confinement impact due to the intervention strategies [17]. Many available confinement models were developed using semi-empirical approaches and were usually derived from concrete [18] or from the classical failure criterions. Confinement models developed for concrete and extended to the masonry have some drawbacks due to the strong variability of the masonries. For this reason a model for all types of masonries is extremely difficult to develop. In this background, the confinement models based on failure criteria appear to be the best approaches to assess the axial capacity of strengthened masonry columns. These models allow to assess the impact of many properties of masonry constituents on the structural performance. Therefore, confinement models able to assess the axial capacity of masonry columns represent important targets.

In this paper, a confinement model, recently particularized by the authors [15] from the failure criterion of Stassi-D'Alia [19, 20] to assess the axial capacity of strengthened masonry, has been discussed remarking its potential as a solid mechanics model. This model was developed according to a failure criterion accounting for the main mechanical parameters representative of the masonry. In order to assess the reliability of the proposed model, other available mechanical models [21] have been used too, to predict the axial capacity of strengthened masonry elements actually tested. The theoretical results of several models have been compared with the experimental results. Finally, in order to confirm the potential of the proposed mechanical model a statistical analysis has been carried out.

CONFINEMENT MODELS

The present paper focuses on confinement models based on a mechanical approach. In particular, the stress state in each point of the material must respect the failure criterion. The failure criterion is based on the definition of boundaries of the failure surface. It can be expressed based on several mechanical parameters representative of materials. This is preferable to assess the impact of several mechanical parameters on the structural behavior of strengthened masonry elements. Furthermore, these models can be easily implemented in Finite Element Modeling (FEM), [22, 23]. The confinement models available in the scientific literature were developed on a failure criterion based on mechanical parameters representative of the confined material. The maximum compressive strength can be assessed by changing the confinement effect (i.e. the lateral or confining stress). For a generic point of the material, the stress state is provided by three components, σ_1, σ_2 and σ_3 along the principal axes, 1, 2, and 3 respectively. The axes 1 and 2 define the main plane where the lateral stresses act (i.e. plane of the cross-section). This internal stress state is due to the confinement effect and depends on the confinement technique. The axis 3 defines the direction where the maximum stress σ_3 increases according to the failure condition (i.e. longitudinal axis of the member). The failure criterion has been applied on masonry elements, therefore in the direction 3 the stress increases up to the compressive strength, f_{m0} (unconfined masonry) and f_{mc} (confined masonry). Conversely, the σ_1 and σ_2 represent the internal stresses provided by the confinement system (under uniform lateral stress $\sigma_1 = \sigma_2$). The envelope of the main stress, σ_3 while changing the lateral stress, σ_1 and, σ_2 provides the confinement curve of the masonry member.

The confinement curve of masonry depends on the compressive and tensile strengths, f_{m0} and f_{mt} respectively. The tensile strength can be expressed in normalized form as the tensile and the compressive strength ratio, $\alpha = f_{mt} / f_{m0}$. This value characterizes the mechanical behavior of the masonry materials. The masonry is made of two main constituents: bricks and mortar and can be modelled according to several approaches: micro or macro-modelling approaches. For this analysis, modelling the masonry, as a whole, appears to be the favorite approach due to the detailed level of analysis. In fact, in order to assess the confinement properties of a masonry element, it can be modelled by using an average behavior between the constituents. For the masonry, the tensile strength is generally governed by the mechanical properties of the mortar. Therefore, the tensile strength of masonry, f_{mt} can be assumed equal to the tensile strength of mortar. Is a normal practice to express the tensile strength as function of the compressive strength of masonry. The tensile strength of masonry as whole can be assumed equal to 10% of its compressive strength for lime mortar and 20% for cementitious

mortars according to experimental results [24, 25]. Conversely, the compressive strength of masonry, f_{m0} is generally assessed by means of compressive tests performed on masonry specimens. The mechanical model based on failure criterion allows to assess the confinement curve under a non-uniform stress state $\sigma_1 \neq \sigma_2$ typically developed in non-axisymmetric confined elements. For these elements, two main lateral stresses can be identified $\sigma_1 = f_{l,\min}$ and $\sigma_2 = f_{l,\max}$. The values, $f_{l,\min}$ and $f_{l,\max}$ depend on the confinement system used for the strengthening strategy. The confinement model depends on these parameters. In fact, for finite element modeling where lateral stresses are usually non-uniform, a mechanical model is essential to account for non-uniform stresses and it can be easily implemented. In the following section, the classical failure criterions were used to derive confinement models.

Drucker-Prager model

The Drucker-Prager model [26] provides the boundaries of the failure surface f_{D-P} as function on the internal stress state, σ_1, σ_2, σ_3 and on the strengths of material (f_{m0} and f_{mt}):

$$f_{D-P}(\sigma_1,\sigma_2,\sigma_3) = \alpha(\sigma_1+\sigma_2+\sigma_3) f_{m0} - \frac{(\sigma_1-\sigma_2)+(\sigma_2-\sigma_3)+(\sigma_1-\sigma_3)}{\sqrt{3}} f_{m0} - \frac{2\alpha}{\sqrt{3}(1-\alpha)} f_{m0} \quad (1)$$

The entire failure surface can be normalized to the compressive strength of masonry f_{m0}. The lateral stresses are the same, $\sigma_1 = \sigma_2 = f_l$ assuming an axisymmetric confinement, where the value, f_l depends on the strengthening system used.

The equation of the failure surface (1) f_{D-P} according to Drucker-Prager model can be written in normalized form, $\overline{f}_{D-P}$, as follows:

$$\overline{f}_{D-P}\left(\overline{\sigma_1}=\overline{\sigma_2}=\frac{f_l}{f_{m0}}, \overline{\sigma_3}=\frac{f_{mc}}{f_{m0}}\right) = \frac{2\alpha}{\sqrt{3}(1-\alpha)} + \frac{(1+\alpha)\left(2\overline{\sigma_1}+\overline{\sigma_3}\right)}{\sqrt{3}(1-\alpha)} - \frac{\sqrt{\overline{\sigma_1}-2\overline{\sigma_1}\,\overline{\sigma_3}-\overline{\sigma_1}^2}}{\sqrt{3}} \quad (2)$$

Fig. 1 shows the three-dimensional failure surface assuming the value α changing from 0 up to 1 with a step of 0.2.

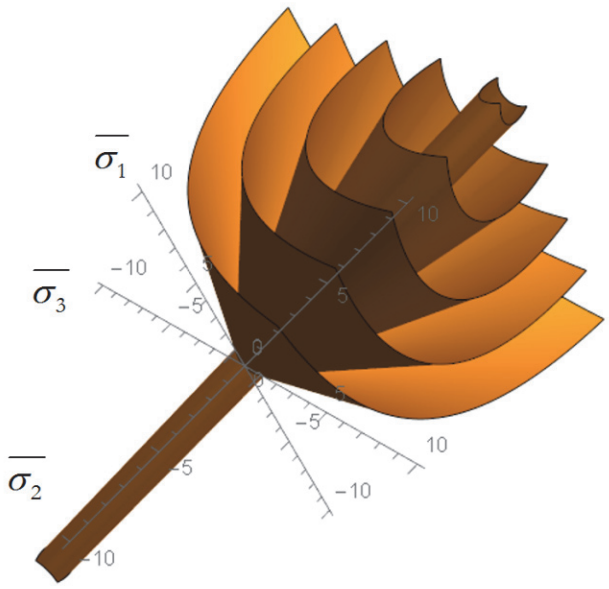

Figure 1: Failure surface according to a Drucker-Prager model assuming α changing from 0 until to 1 with a step of 0.2.

In the Eqn. (1) the confinement effect is provided by the lateral stresses $\sigma_1 = \sigma_2$; while, σ_3 represents the axial stress applied on the masonry columns. The confinement curve is provided by the maximum σ_3 related to the lateral stress state $\sigma_1 = \sigma_2$ (i.e. the confinement effect). In particular, the Eqn. (2) provides a second order equation in the unknown parameter, σ_3. In order to obtain the confinement curve, only the compressive component must be considered for the analysis:

$$\overline{\sigma_3} = 1 - \left(\frac{3+\alpha}{2\alpha}\right)\overline{\sigma_1} \tag{3}$$

The Eqn. (3) can be used to assess the confinement curve of strengthened masonry columns. It represents one solution (maximum compressive stress) of the algebraic Eqn. (2). The second solution regards the negative value of the stress σ_3 (i.e. tensile stress), useless for this discussion.

Stassi-D'Alia model

The Stassi-D'Alia model [19, 20] provides the boundaries of the failure surface, f_{S-D} with the following equation:

$$f_{S-D}(\sigma_1,\sigma_2,\sigma_3) = -f_{m0}(1+\alpha)(\sigma_1+\sigma_2+\sigma_3) + \left(\sigma_1^{\,2}+\sigma_2^{\,2}+\sigma_3^{\,2}-\sigma_1\sigma_2-\sigma_2\sigma_3-\sigma_1\sigma_3\right)f_{m0} + \alpha f_{m0}^{\,2} \tag{4}$$

The Eqn. (4), assuming an axisymmetric confinement, can be rewritten in normalized form as follow:

$$\overline{f}_{S-D}\left(\overline{\sigma_1}=\overline{\sigma_2}=\frac{f_l}{f_{m0}},\overline{\sigma_3}=\frac{f_{mc}}{f_{m0}}\right) = \alpha + \overline{\sigma_1}^{\,2} - 2\overline{\sigma_1}\,\overline{\sigma_3} + \overline{\sigma_3}^{\,2} - (1+\alpha)\left(2\overline{\sigma_1}+\overline{\sigma_3}\right) \tag{5}$$

Fig. 2 shows the three-dimensional failure surface assuming the value, α changing from 0 up to 1 with a step of 0.2.

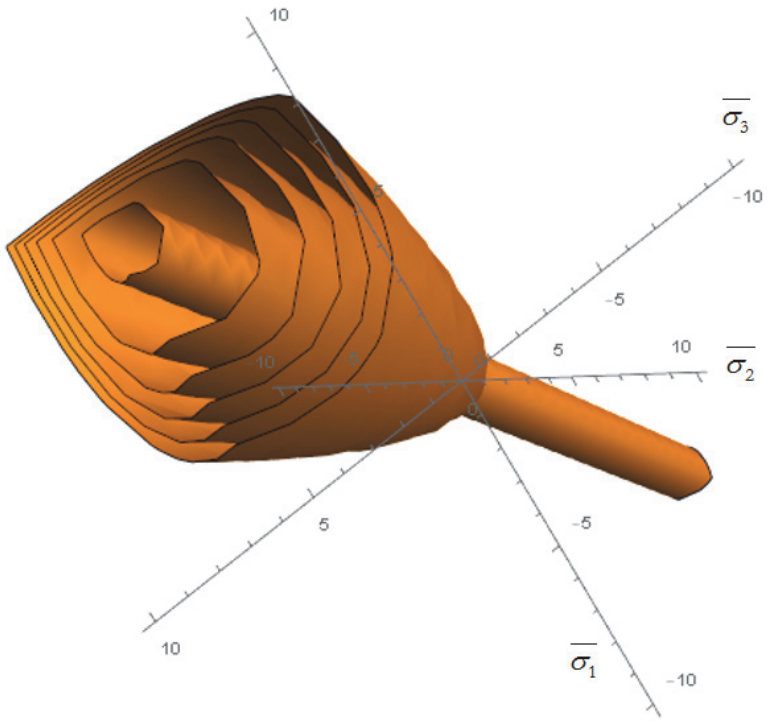

Figure 2: Failure surface according to a Stassi-D'Alia model assuming α changing from 0 up to 1 with a step of 0.2.

The Eqn. (5) is an algebraic second order equation in the unknown parameter, σ_3. The positive solution of the previous equation provides the maximum compressive strength, σ_3 for different lateral stress states $\sigma_1 = \sigma_2$:

$$\overline{\sigma_3} = \frac{1}{2}\left(1 + \alpha + 2\overline{\sigma_1} + \sqrt{1 - 2\alpha + \alpha^2 + 12\overline{\sigma_1} + 12\alpha\overline{\sigma_1}}\right) \tag{6}$$

The envelope of the σ_3 points to change the internal lateral stress state $\sigma_1 = \sigma_2$ represents the confinement curve.

Henky-Von Mises model

Henky-Von Mises model [27, 28] was developed for homogeneous materials with compressive strength, f_{m0} equal to the tensile strength, f_{mt} (i.e. $\alpha = 1$). This assumption is certainly not justified for the masonry, where $\alpha < 1$, but it is interesting in order to assess the drawbacks of the other models. This model provides the boundaries of the failure surface by means of the following equation:

$$f_{H-VM}(\sigma_1, \sigma_2, \sigma_3) = \left(\sigma_1^2 + \sigma_2^2 + \sigma_3^2\right) f_{m0} - \left(\sigma_1\sigma_2 + \sigma_2\sigma_3 + \sigma_1\sigma_3\right) f_{m0} - f_{m0}^2 \tag{7}$$

The Eqn. (7), expressed in normalized form and under an uniform lateral stress state, becomes:

$$\overline{f}_{H-VM}\left(\overline{\sigma_1} = \overline{\sigma_2} = \frac{f_l}{f_{m0}}, \overline{\sigma_3} = \frac{f_{mc}}{f_{m0}}\right) = -1 + \overline{\sigma_1}^2 - 2\overline{\sigma_1}\,\overline{\sigma_3} + \overline{\sigma_3}^2 \tag{8}$$

Fig. 3 shows the three-dimensional failure surface model independent on α.

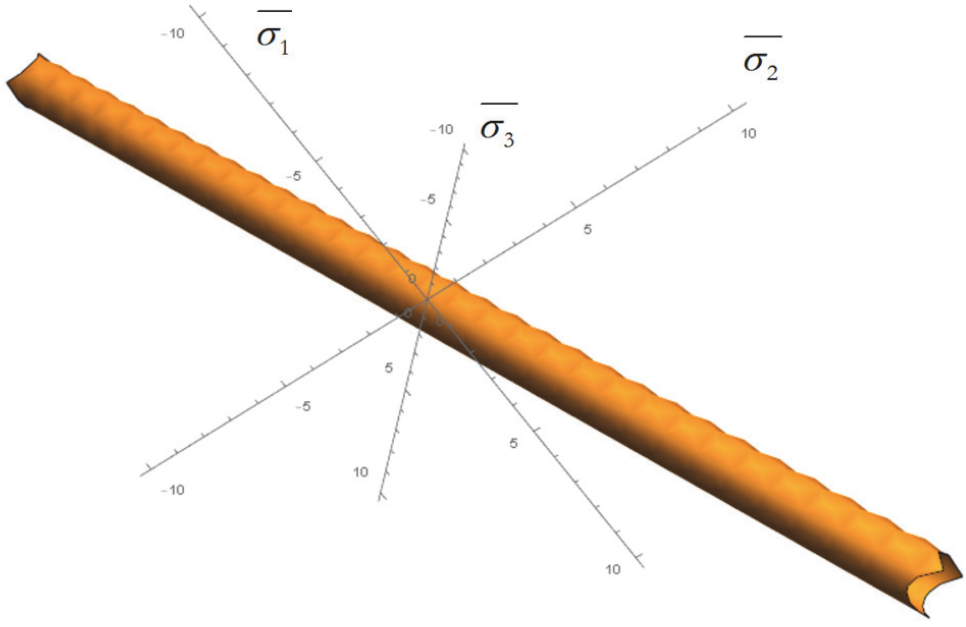

Figure 3: Failure surface according to a Henky-Von Mises model independent on α.

The solution of the Eqn. (8) for confinement is represented by the positive stress, σ_3:

$$\overline{\sigma_3} = 1 + \overline{\sigma_1} \tag{9}$$

Mohr-Coulomb model

Mohr-Coulomb model [29, 30] provides the boundaries of the failure surface by means of the intersection of six planes:

$$\begin{aligned}
\pm\frac{\sigma_1-\sigma_2}{2} &= -\left(\frac{\sigma_1+\sigma_2}{2}\right)\sin\phi + c\cdot\cos\phi \\
\pm\frac{\sigma_2-\sigma_3}{2} &= -\left(\frac{\sigma_2+\sigma_3}{2}\right)\sin\phi + c\cdot\cos\phi \\
\pm\frac{\sigma_3-\sigma_1}{2} &= -\left(\frac{\sigma_3+\sigma_1}{2}\right)\sin\phi + c\cdot\cos\phi
\end{aligned} \tag{10}$$

where: ϕ is the friction angle and c is the cohesion of material. These mechanical parameters can be expressed as function of the compressive and tensile strengths. The failure surface can be normalized to the compressive strength of masonry, f_{m0}. Not all planes must be considered to describe the confinement curve of the strengthened masonry elements. In particular, the firsts two equations of the algebraic system (10) can be neglected since they do not contain the axial stress, σ_3. The remaining Eqns. (10) provide solutions grouped two by two. Therefore, only two equations are sufficient to describe the boundaries of the failure surface. These equations can be rewritten according to a uniform lateral stress state and in normalized form as follows:

$$\begin{aligned}
\overline{f}'_{M-C}\left(\overline{\sigma_1}=\overline{\sigma_2}=\frac{f_l}{f_{m0}},\overline{\sigma_3}=\frac{f_{mc}}{f_{m0}}\right) &= \frac{\overline{\sigma_2}-\overline{\sigma_3}}{2}+\frac{\overline{\sigma_2}+\overline{\sigma_3}}{2}\left(\frac{1+\alpha}{1-\alpha}\right)-\frac{\alpha}{1-\alpha} \\
\overline{f}''_{M-C}\left(\overline{\sigma_1}=\overline{\sigma_2}=\frac{f_l}{f_{m0}},\overline{\sigma_3}=\frac{f_{mc}}{f_{m0}}\right) &= \frac{\overline{\sigma_3}-\overline{\sigma_1}}{2}+\frac{\overline{\sigma_3}+\overline{\sigma_1}}{2}\left(\frac{1+\alpha}{1-\alpha}\right)-\frac{\alpha}{1-\alpha}
\end{aligned} \tag{11}$$

Fig. 4 shows the three-dimensional failure surface assuming the value, α changing from 0 up to 1 with a step of 0.5.

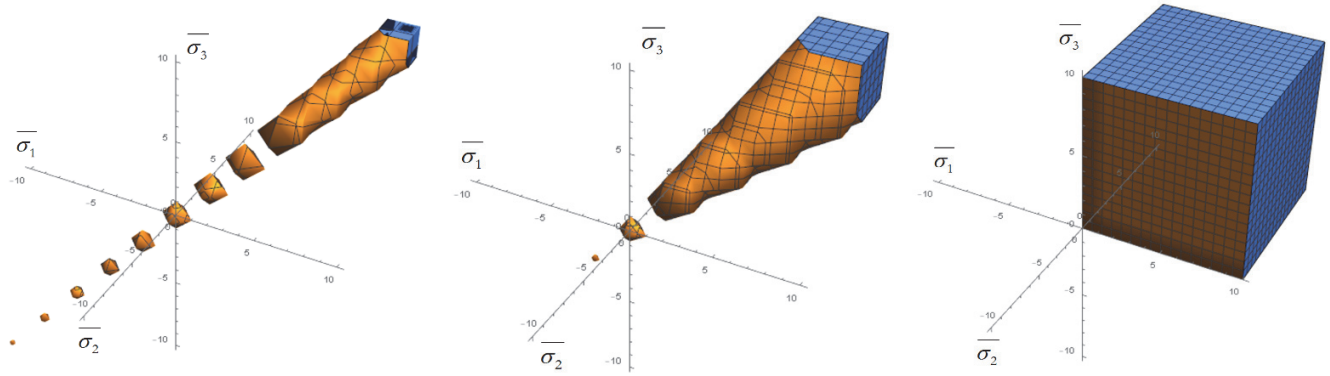

Figure 4: Failure surfaces according to a Mohr-Coulomb model assuming α changing from 0 up to 1 with a step of 0.5.

In order to assess the confinement performance, the solution of the (11) must be focused on the compressive stress only, as follows:

$$\overline{\sigma_3}=1-\frac{1}{\alpha}\overline{\sigma_1} \tag{12}$$

CONFINING STRESS ESTIMATION

The experimental results have been compared with the theoretical predictions. The confinement curve provides the confined masonry strength, f_{cm} while changing the confining stress, f_l due to the passive confinement. The confining stress, f_l can be assessed by using several formulations [31, 32]. In this paper, two approaches

have been adopted to calculate the confining stress, f_l. The effective confining stress (namely $f_{l,eff}$) depends on additional parameters not involving the characteristics of the composite system. Semi-empirical formulations available in the scientific literature provide this stress as a function of key efficiency parameters. According to classical formulation [31] the effective confining stress, $f_{l,eff}$ under passive confinement, can be assessed as follow:

$$f_{l,eff} = f_l \cdot k_{eff} = \frac{1}{2} \cdot \rho_f \cdot E_f \cdot \varepsilon_f \cdot k_{eff} \tag{13}$$

where, E_f is the Young's modulus of the fiber, ε_f is the ultimate design strain of the fiber (for the following experimental comparisons, it is equal to the average ultimate strain, without any safety factor) and ρ_f is the confinement volumetric ratio of the strengthening system. The calculation of ρ_f depends on the characteristics of the strengthened cross section:

$$\rho_f = \frac{4 \cdot t_f \cdot b_f}{D \cdot p_f} \quad \text{for circular wrapped cross-section} \tag{14}$$

$$\rho_f = \frac{4 \cdot t_f \cdot b_f}{\max(b,d) \cdot p_f} \quad \text{for rectangular cross-section} \tag{15}$$

where, t_f is the thickness of the confined layer, b_f is the width of the wrap, p_f is the spacing between the wraps, D is the diameter of the circular cross-section, b and d are the dimensions of the rectangular cross-section.
The coefficient, k_{eff} depends on efficiency of the strengthening system; it can be assumed as follow:

$$k_{eff} = k_h \cdot k_v \cdot k_\alpha \tag{16}$$

where the three coefficients, k_h, k_v and k_α can be easily assessed according to the formulations reported in the CNR guidelines [31]. They depend on geometrical and mechanical parameters; k_h is the coefficient of horizontal efficiency:

$$k_h = 1 - \frac{b'^2 + d'^2}{3 \cdot A_m} \tag{17}$$

where the dimensions b' and d' provide the sizes of the effectively confined core (external dimensions minus the radii of the rounded corners), and A_m is the area of the gross cross-section and assumes unitary value also for circular confined columns. The coefficient k_v represents the vertical efficiency that assumes unitary value for continuous wrapping systems ($b_f = p_f$). The coefficient k_α is the efficiency due to the inclination of the fibers. In the present paper, the strengthening was carried out without inclination of fibers, justifying the assumption of $k_\alpha = 1$.
A second approach [32] has been used to estimate the lateral stress, $f_{l,eff}$ on the confined members, as follows:

$$f_{l,eff} = f_l \cdot k_{eff} = 2\frac{b+d}{b \cdot d} \cdot t_f \cdot E_f \cdot \varepsilon_f \cdot k_{eff} \tag{18}$$

For circular confined cross-sections, the dimensions, b and d assume the value of the diameter, D. The coefficient, k_{eff} can be calculated with the same previous formulations [31].

EXPERIMENTAL RESULTS

Several experimental programs, taken from the technical literature, have been considered. The reliability of the confinement models previously discussed has been checked by comparison between the theoretical predictions and experimental results. Experimental tests were carried out on masonry specimens strengthened with several types of strengthening systems. The attention focused on masonry columns made of solid and cored clay bricks tested under pure axial load (a total of 67 tests were collected). The axial capacity of these masonries was improved with several strengthening strategies. Present work focused on strengthening systems made of organic matrix (i.e. epoxy-resin) and different types of fibers (basalt, carbon and glass) namely Basalt Fiber Reinforced Polymer (BFRP), Carbon Fiber Reinforced Polymer (CFRP) and Glass Fiber Reinforced Polymer (GFRP) respectively. The masonry columns considered in the experimental programs are characterized by rectangular and circular cross-sections with different scale factors.

The experimental programs were conducted by using different techniques. In experimental tests, the confinement on a masonry specimen can be provided by means of active or passive systems. The active confinement is applied in the laboratory by means of specific machines. Under uniform axial load, the increasing of the axial load provides a transverse (restrained by the wrapping) dilatation producing a passive confinement. Therefore, the efficiency of the passive confinement is strongly influenced by the characteristics of the masonry substrate and the strengthening system. For masonry columns passively confined, the failure condition is generally due to the failure of the wraps. In following section a synthetic description was provided of the experimental programs used for the comparison between the experimental results and the numerical predictions. Additional information on the specimens and experimental results were reported in the appendixes A and B.

In Faella et al. [33], fiftyfour masonry specimens with different texture, dimensions and constituents were tested under pure axial load. A pozzolan based mortar was used for all masonry specimens (Tab. 1.A). The specimens were strengthened by using several types of strengthening systems having mechanical characteristics shown in Tab. 1.A. Seventeen masonry specimens made of two types of solid clay bricks were considered for the theoretical and numerical comparison. The two types of masonries present mass densities equal to 1650 kg/m^3 and 1700 kg/m^3 respectively and different dimensions as shown in Tab. 1.B. They were wrapped with different number of plies (one or two) and different types of GFRP (namely type a and type b as shown in Tab. 1.A). The density and thickness of fibers are equal to 900 g/m^2 and 0.23 mm/ply respectively.

In Di Ludovico et al. [34] eighteen passive confinement tests were performed on scaled and not scaled down masonry columns. Only the experimental results on clay brick masonry (Tab. 2.A) have been included in the present analysis. The tests were performed under pure axial load on masonry columns strengthened with several types of composites (Tab. 2.A). Six tests were carried out on square clay masonry columns with dimensions shown in Tab. 3.B. For this group the clay brick presents sizes of 55×115.5×255 mm^3, while the thickness of joints was reduced at 12 mm due to the scale effects. The masonry had a mass density equal to 1700 kg/m^3. The specimens were strengthened by using uniform wrapping with synthetic fibers (GFRP and BFRP composite systems). The confinement tests were carried out according to displacement control with rate of 0.005 mm per second. The failure mode was due to the composite for the entire set of specimens. Three of the six specimens were wrapped with one ply of composite based on Glass fiber (GFRP) having density and thickness of fiber equal to 900 g/m^2 and 0.48 mm/ply respectively. Three specimens were wrapped with one ply of strengthening system based on basalt fibers (BFRP) having mass density and thickness equal to 254 g/m^2 and 0.24 mm/ply respectively. Further information were reported in the Tab. 2. A.

In Alecci et al. [35] tri-axial compression tests were performed on nineteen specimens. Three of the nineteen specimens made of pressed clay bricks (Tab. 3.A) of 65×30×14 mm^3 dimensions were tested using passively confinement. Then cylindrical specimens with diameter of 54 mm were obtained from elements of 250×120×50 mm^3. They were cut in 14 mm thick slices and successively divided in two semicircular shaped bricks. The joints were made of lime mortar with reducing granulometry to respect the scale factor. The final cylindrical specimens had height of 85 mm and reduced thickness of joints of 2.5 mm due to the scale factor (Tab. 5.B). The specimens were wrapped with CFRP (Tab. 3.A) composite characterize by different volumetric ratio of fiber (Tab. 5.B). It was obtained fixed the type of composite and changing the equivalent thickness as shown in Tab. 5.B. The unconfined compressive strength was assessed by means of direct test (Tab. 3.A). The failure mode occurs by means of the progressive increasing of the axial load with a load rate equal to 0.2 MPa per second. These conditions were the same for each specimen and the failure mode occurred due to cracking of the composite system.

In Bieker et al. (2002) [36] eight masonry specimens were tested under pure axial load. Two types of masonry (solid and hollow bricks) were considered to perform the confinement tests. The solid clay brick had dimensions of 71×115×240

mm³ and 113×115×240 mm³ for the solid and hollow masonry respectively. The masonries present mass density of 2000 kg/m³ and 900 kg/m³ for solid and hollow bricks respectively. The masonry was prepared using two types of mortar: calcium mortar (namely type a) and cement mortar (namely type b). Brick and mortar were coupled in order to get a realistic representation of the existing masonries. The specimens were wrapped using two types of strengthening systems based on synthetic fiber (carbon and glass) and epoxy-resin. The carbon was applied using sheets having a mass density of 230 g/m². Conversely, the glass fiber was applied using an unidirectional fiber system with a mass density of 430 g/m². The wrapping was applied by means of one or two plies of CFRP, and two and three plies of GFRP with resin interlayers. The mechanical characteristics and the geometries of specimens were shown in Tabs. 4.A and 7.B respectively.
In Rao et al. [37] seventyeight specimens were involved in the experimental investigation. The attention focused on standard specimens made of solid and cored clay bricks (Tab. 5.A). The mortar joint thickness changed between 10 and 12 mm (Tab. 9.B). The specimens were wrapped by CFRP and GFRP having 200 g/m² and 200-360 g/m² respectively (Tab. 5.A). One ply of CFRP and GFRP (Tab. 5.A) was wrapped around the specimens. The failure of specimens occured at increasing axial load, under displacement control at rate of 0.01mm per second.
In Corradi et. al. [38] twentyfour masonry columns made of solid clay brick were tested under pure axial load. Two types of masonry were considered for the experimental program (Tab. 6.A). The geometrical characteristics were reported in the Tab. 11.B. The attention focused on four masonry specimens strengthened using several strengthening systems (Tab. 6.A). The solid clay bricks with dimensions of 245×120×55 mm³ were used to assembly the masonry specimens. The mortar used was composed of Portland cement and hydraulic lime. The thickness of mortar was fixed to 8-10 mm. The specimens were wrapped with strengthening systems made of organic matrix (epoxy resin) and synthetic fiber with different mechanical properties (Tab. 6.A). Two types of fibers were considered for the passive confinement: carbon with high tensile strength (CFRP-HT) and carbon fiber with very high modulus (CFRP-VHM).
In Krevaikas et al. [39] fortytwo masonry specimens made of solid clay brick were tested (Tab. 7.A) by means of pure axial load tests. For the analysis, six specimens were considered to compare the numerical results with the theoretical previsions. The brick element had dimensions of 55×40×115 mm³ coupled with a mortar cement and lime based. The specimens were prepared according to several scale factors (1:1, 1.5:1 and 2:1) providing specimens with dimensions 115×115×340 mm³, 172.5×115×340 mm³ and 130×115×340 mm³. The thickness of mortar was fixed to 10 mm for all specimens. Two types of strengthening systems were considered: GFRP and CFRP (Tab. 7.A). The specimens were wrapped with one, two and three plies of unidirectional CFRP sheets or with five plies of unidirectional GFRP system (Tab. 13.B). The fiber system was applied on the substrate using epoxy-resin.
In Aiello et al. (2009) [40] thirtythree masonry specimens were tested under pure axial load. For the present study one specimen was considered due to the similarity with previous experimental programs (Tab. 8.A). The specimen was made of solid clay bricks having dimensions shown in Tab. 15.B. It was prepared starting from blocks with dimensions of 100×150×30 mm³. A mortar lime and cement based was used for the masonry specimen. It was wrapped with GFRP system with one plie and epoxy-resin (Tab. 8.A).
The further information on the mechanical properties of constituents used in the past experimental programs previously outlined were reported in the Appendix A, from Tab. 1.A to Tab. 8.A. The geometrical characteristics of the specimens (cross-section, b×h and height, h), characteristics of strengthening systems (type of fiber, number of layers, n_l, equivalent thickness, t_{eq}) and the experimental results in terms of unconfined, f_{m0} and confined compressive, f_{mc} strengths, are reported in Appendix B. The confined compressive strength, f_{mc} can be normalized to the unconfined compressive strength, f_{m0}, as shown in Appendix B. For each specimen, the effective confining stress, $f_{l,eff}$ has been assessed according to the two approaches previously discussed (Eqns. 13 and 18). The effective confining stress, $f_{l,eff}$ has been expressed in normalized form as shown in the Appendix B, from Tab. 1.B to Tab. 16.B. The additional results of the experimental tests are available in the original papers [33-40].

STATISTICAL PARAMETERS FOR THE COMPARISON OF RESULTS

The reliability of the mechanical models previously discussed has been tested by comparing the theoretical previsions with the experimental results. Some statistical parameters have been chosen to assess the reliability of the available confinement models. The comparison has been performed by means of some statistical parameters. The absolute approximation provides first information on the local reliability of the confinement models and it can be calculated as follow:

$$e = \left| \frac{\overline{f_{\exp,i}} - \overline{f_{th,i}}}{\overline{f_{\exp,i}}} \right| \tag{19}$$

where, $\overline{f_{\exp,i}}$ and $\overline{f_{th,i}}$ represent the experimental and theoretical values for the generic specimen, i respectively. In particular they represent the compressive strength of the confined masonry specimen derived by the experimental and theoretical results. They are generally normalized to the unconfined compressive strength of the masonry specimen. However, the approximation parameter provides local information without considering the entire sample. Therefore it cannot be used to assess the performance of mechanical models. Three statistical parameters can be used to assess the entire sample of the experimental results: the mean absolute percentage error (MAPE), mean square error (MSE) and coefficient of determination (R^2). These statistical parameters allow to compare the theoretical prediction with the experimental results on the entire statistical sample. The statistical parameters can be calculated as follow:

$$MAPE = \frac{\sum_{i=1}^{n} \left| \frac{\overline{f_{\exp,i}} - \overline{f_{th,i}}}{\overline{f_{\exp,i}}} \right|}{n} \tag{20}$$

$$MSE = \frac{\sum_{i=1}^{n} \left(\overline{f_{\exp,i}} - \overline{f_{th,i}} \right)^2}{n} \tag{21}$$

$$R^2 = 1 - \left(\frac{\sum_{i=1}^{n} \left(\overline{f_{\exp,i}} - \overline{f_{th,i}} \right)^2}{\sum_{i=1}^{n} \overline{f_{th,i}}} \right) \tag{22}$$

where, n is the number of specimens for each confinement test. The prediction models provide reliable results when:

$$MAPE \to 0$$
$$MSE \to 0$$
$$R^2 \to 1$$

THEORETICAL AND EXPERIMENTAL COMPARISON RESULTS

The reliability of mechanical models previously derived by the available failure criteria has been discussed in the following section, by comparing the experimental results with the theoretical previsions. The analysis was carried out in terms of direct comparison between the experimental and theoretical results and in terms of confinement curves. A first step has been carried out by comparing the confined compressive strength, f_{mc} normalized to the unconfined compressive strength, f_{m0}, experimentally evaluated with the same ratio calculated using the theoretical models.

No specific information is provided in original papers on tensile strength of masonry as a whole. Tensile strength is preferably retrieved by direct or indirect experimental tests [41] or correlations with other mechanical properties [40]. Compressive strength of the mortar only was reported and the tensile strength of masonry is assumed equal to 10% of compressive strength for lime mortar and 20% for cementitious mortars. The values of α assumed for each experimental program are shown in Tab. 1.

The direct comparison between the experimental results and the theoretical previsions is a useful tool to assess the response of the model on the entire experimental sample. It can be performed on a diagram where in the horizontal axIs is shown the normalized confined compressive strengths, theoretically assessed; while on the vertical axis is reported the

same value experimentally assessed. On this diagram, the ideal line is represented by a linear function with unitary angular coefficient. The points located at left of the ideal line (dashed grey line of following figures) correspond to theoretical values lower than the experimental results. Therefore, if the sample points shift at left of the ideal line, the theoretical model provides conservative results.

Experimental program	α[-]
Faella et al. (2011)	-0.1
Di Ludovico et. al. (2010)	-0.1
Alecci et al. (2009)	-0.1
Bieker et al. (2002)	-0.1(solid clay), -0.2(cored clay)
Nanjunda Rao et al. (2014)	-0.2
Corradi et al. (2007)	-0.2
Krevaikas et al. (2005)	-0.2
Aiello et al. (2009)	-0.2

Table 1: Value of the normalized tensile strength of masonry, α for the experimental programs.

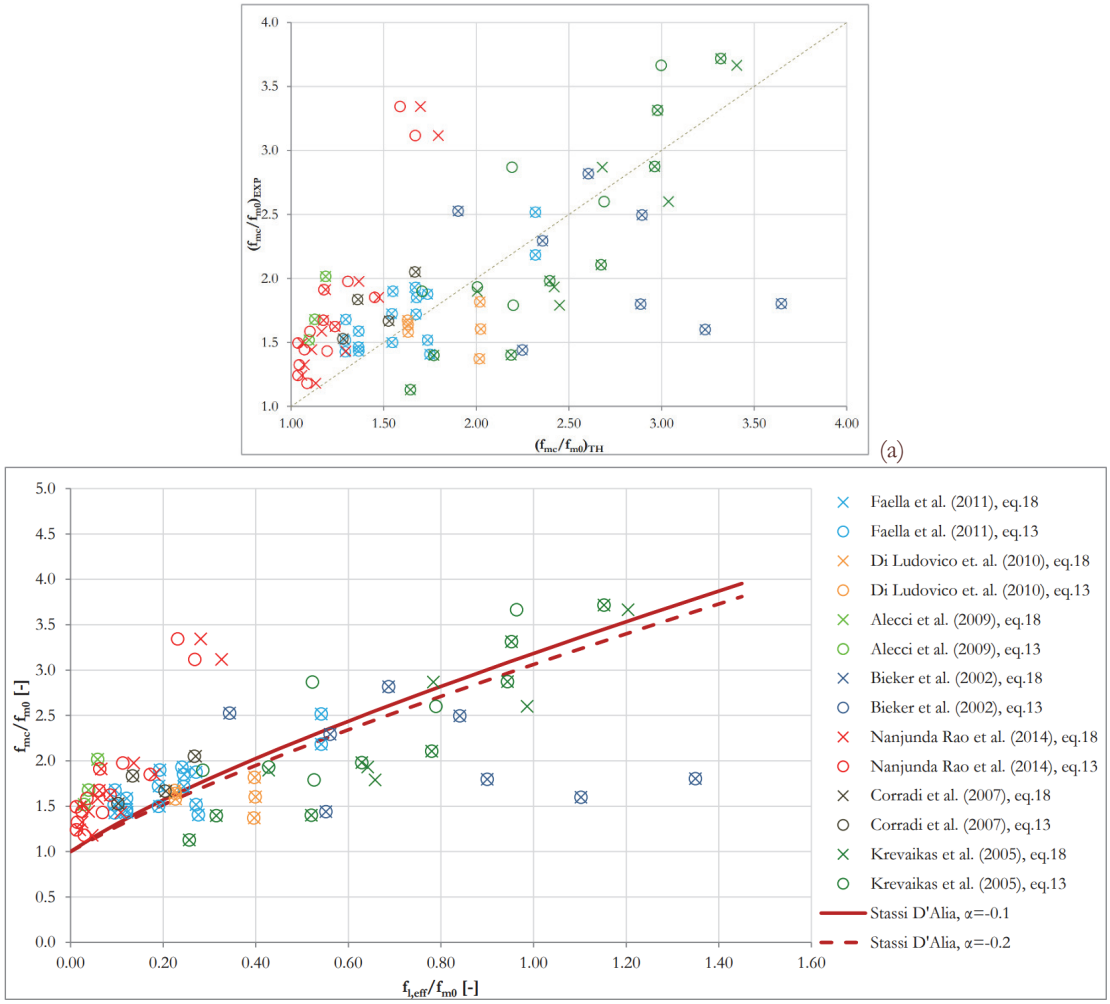

Figure 5: Comparison between experimental results and Stassi-D'Alia model: a) experimental and theoretical results comparison, b) confinement curve comparison for α =-0.1 (red solid line) and α =-0.2 (red dashed line).

Another important information can be assessed with the confinement curves. They provide the confined compressive strength while changing the effective confining stress, normalized to the unconfined compressive strength. The theoretical confinement curves are shown for two values of the normalized tensile strength of masonry, α fixed at -0.1 (dashed line) and -0.2 (solid line) according to the experimentally calculated values. Fig. 5 a) shows the comparison between the Stassi-D'Alia model and the experimental results; while the Fig. 5 b) shows the theoretical confinement curves with the several experimental points. The effective confining stress has been evaluated according to the approaches previously discussed (Eqns. 13 and 18, howsoever it is remarked that in the case of square cross sections the results are equal).
Comparing this model with the experimental sample, the good fitting of the theoretical results with the experimental results is clear. In particular, the Stassi-D'Alia model provides reliable results for the entire experimental sample without excessive overestimation of the theoretical previsions (Fig. 5 a). The theoretical results confirm that the confinement curve is weakly influenced by the tensile strength of masonry. It is interesting to note that the mechanical model reasonably predicts the axial capacity for the entire range of the lateral stress field.
The same approach has been carried out for other theoretical models. Fig. 6 a) shows the comparison between the Drucker-Prager model and the experimental results; while Fig. 6 b) shows the theoretical confinement curves with the experimental points.

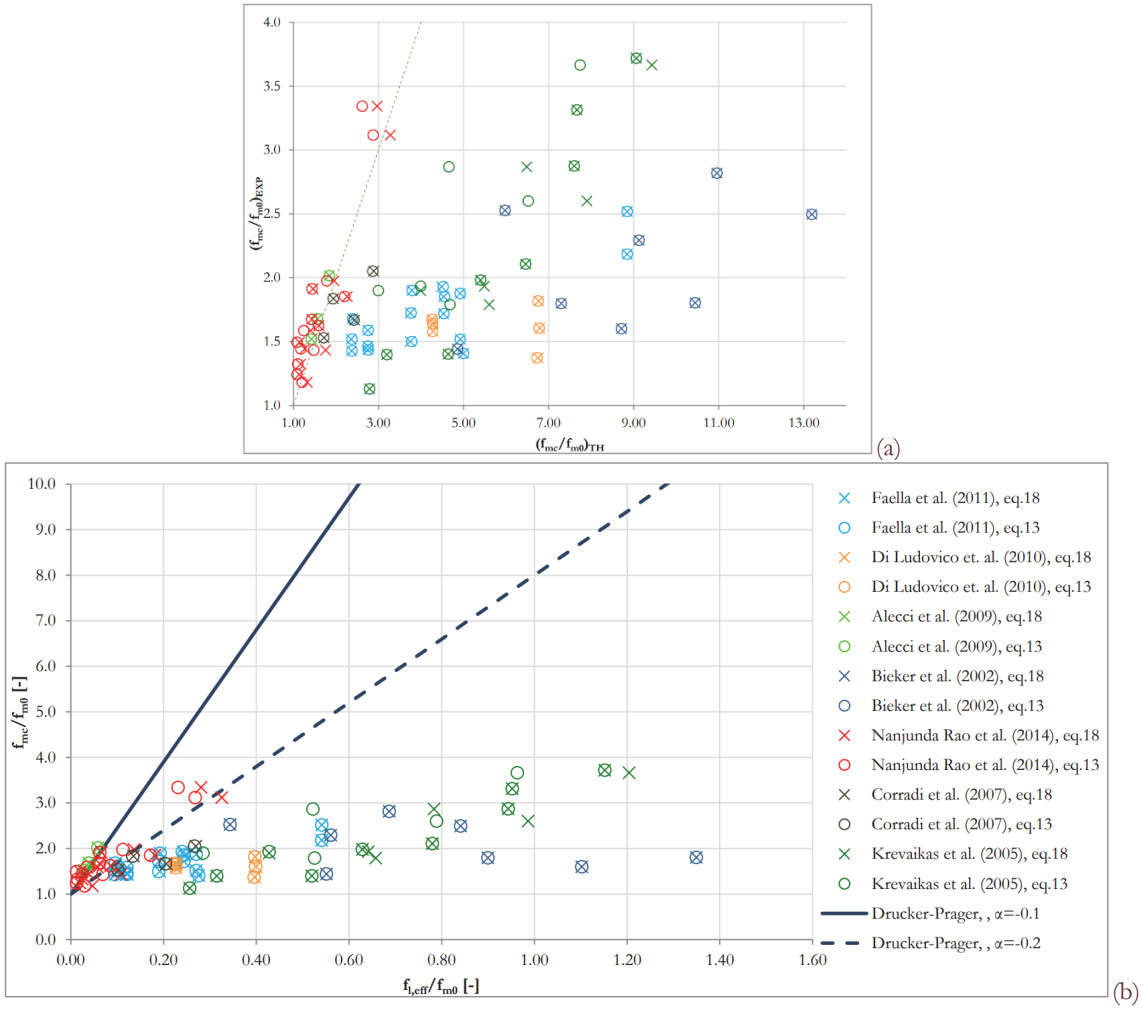

Figure 6: Comparison between experimental results and Drucker-Prager models: a) experimental and theoretical results comparison, b) confinement curve comparison for α =-0.1 (blue solid line) and α =-0.2 (blue dashed line).

This model strongly overestimates the experimental results as shown in Fig. 6 a). In particular, this effect is very clear for high values of the confining stress. In fact, for low confining stresses, $f_{l,eff}/f_{m0} < 0.2$ the mechanical model provides reliable results if compared with the experimental tests. However, a great number of tests were carried out at high

confining stress values. Therefore, on the entire experimental sample the model provides a weak estimation of the axial capacity of masonry columns wrapped with composites. Furthermore, it results strongly influenced by the tensile strength of masonry providing confinement curves strongly different while changing the tensile strength of masonry. Fig. 7 a) shows the comparison between the Hencky-Von Mises model and the experimental results; while Fig. 7 b) shows the comparison between the theoretical confinement curves and the experimental points.

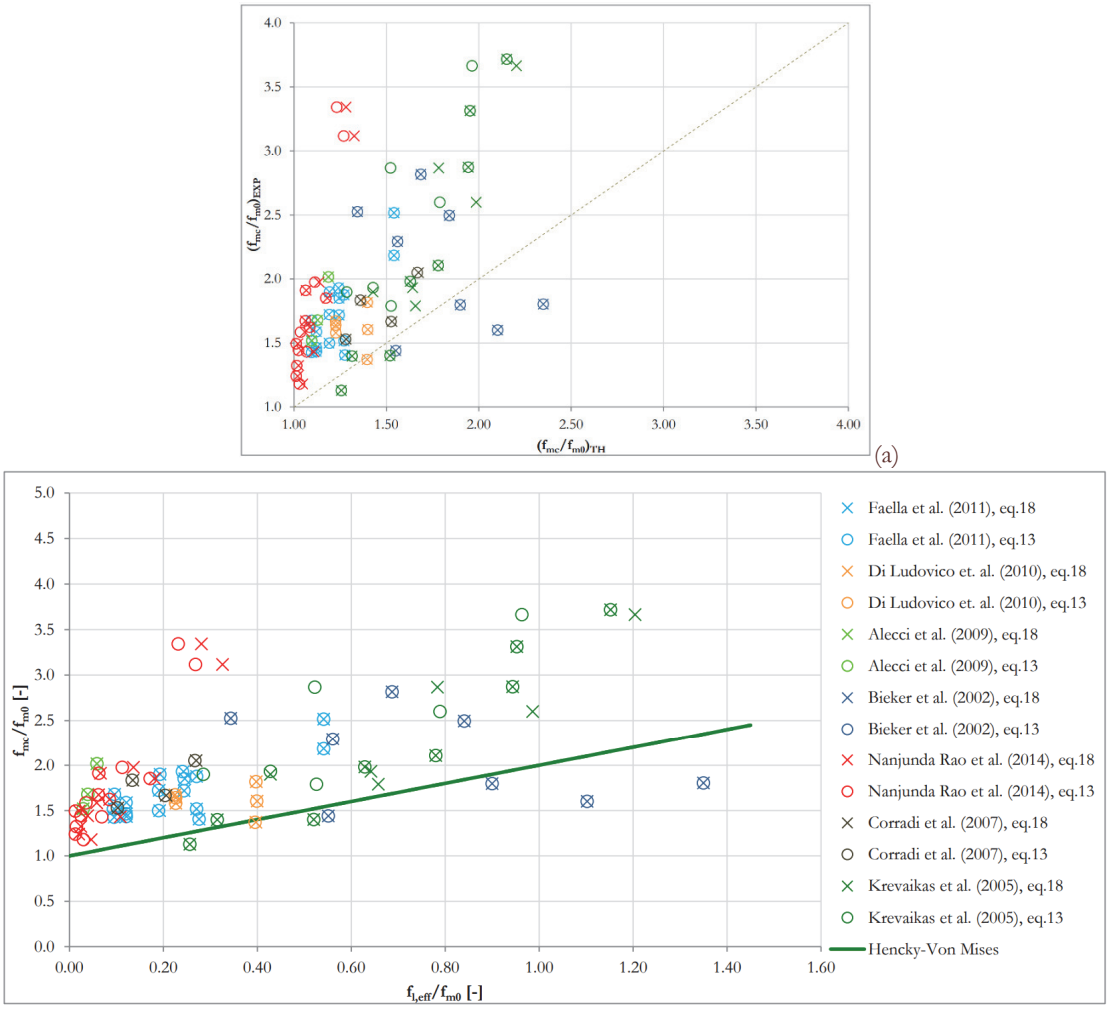

Figure 7: Comparison between experimental results and Hencky-Von Mises models: a) experimental and theoretical results comparison, b) confinement curve comparison independent on α.

This model does not depend on the normalized tensile strength of confined material, α. The theoretical and experimental comparison shows a clear underestimation of the experimental values. This effect is clear for the entire confining stress field. The Fig. 8 a) shows the comparison between the Mohr-Coulomb model with the experimental results; while Fig. 8 b) shows the comparison between the theoretical confinement curves with the experimental points.
This theoretical model is strongly influenced by the normalized tensile strength of masonry, α. Furthermore, an overestimation of the experimental results is clear for the entire experimental example sample. Also for low values of the effective confining stresses the experimental results are not so well fitted by the theoretical results (Fig. 8 a).
In order to confirm previous qualitative dissertation, the statistical parameters: MAPE, MSE and R^2 have been calculated for the mechanical models. They are shown in Tabs. 2 and 3 for the comparison between the experimental and theoretical results. The effective confining stress, $f_{l,eff}$ has been calculated according to the previous Eqns. (13) and (18). The statistical parameters calculated according to Eqns. (13) and (18) are shown in Tab. 26 and 27 respectively.

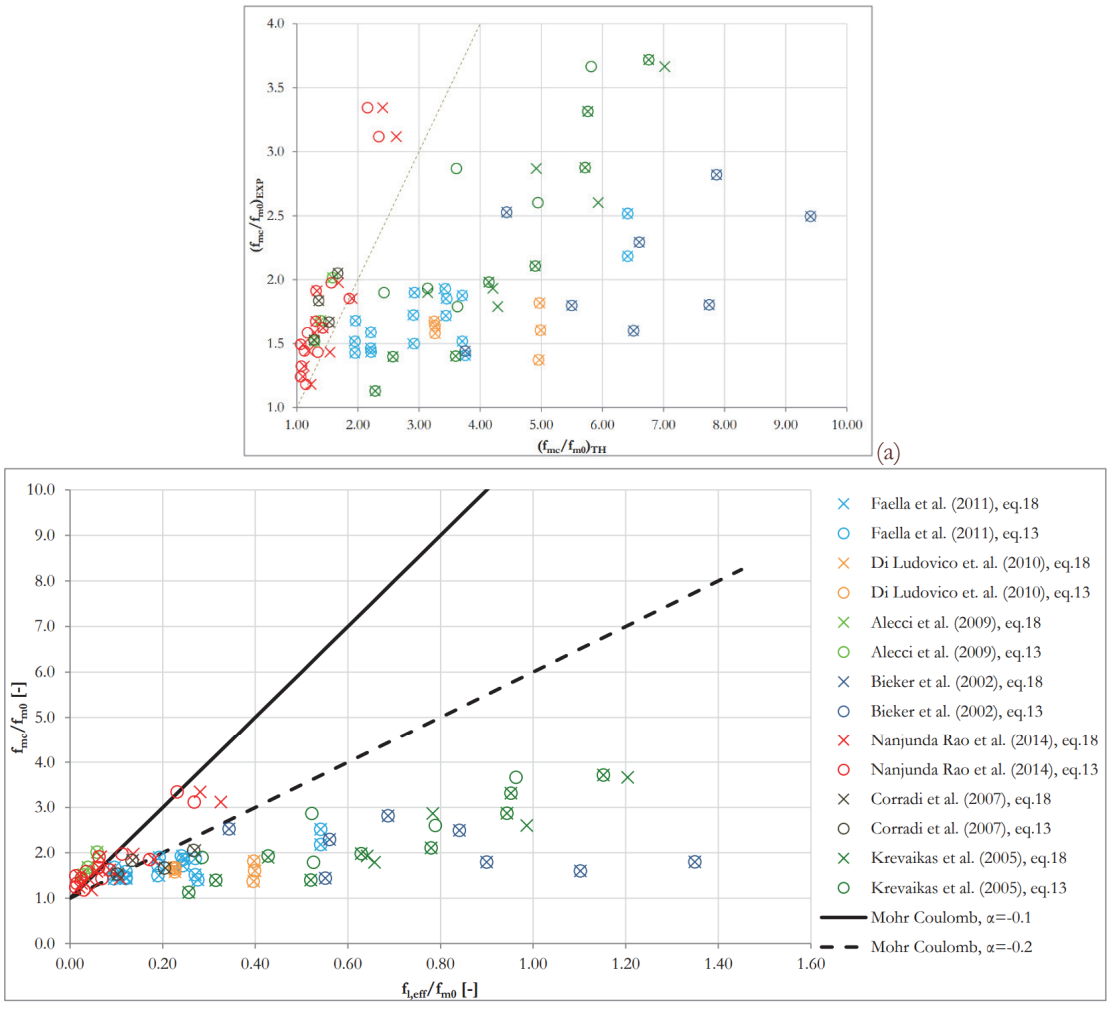

Figure 8: Comparison between experimental results and Mohr-Coulomb models: a) experimental and theoretical results comparison, b) confinement curve comparison for α =-0.1 (black solid line) and α =-0.2 (black dashed line).

Statistical parameter	Stassi-D'Alia	Drucker-Prager	Henky-Von Mises	Mohr-Coulomb
MAPE	0.225	1.324	0.289	0.855
MSE	0.328	12.481	0.535	5.075
R^2	0.820	-1.86	0.603	-0.512

Table 2: Statistical parameters to comparison the theoretical and the experimental results, with a confined lateral stresses, $f_{l,eff}$ calculated according to Eqn. (13).

Statistical parameter	Stassi-D'Alia	Drucker-Prager	Henky-Von Mises	Mohr-Coulomb
MAPE	0.243	1.375	0.280	0.887
MSE	0.311	13.342	0.496	5.419
R^2	0.833	-1.954	0.800	-0.563

Table 3: Statistical parameters to comparison the theoretical and the experimental results, with a confined lateral stresses, $f_{l,eff}$ calculated according to Eqn. (18).

The assessment of the statistical parameters confirms the reliability of the Stassi-D'Alia model compared to others. It is interesting to note that the model is weakly depended on the formulation - eqs. (13) versus (18) - used for the effective confining stress, $f_{l,eff}$ (Fig. 9). Hence, the statistical results confirmed the Stassi-D-Alia model to be the best analytical tool to assess the axial capacity of confined clay brick masonry.

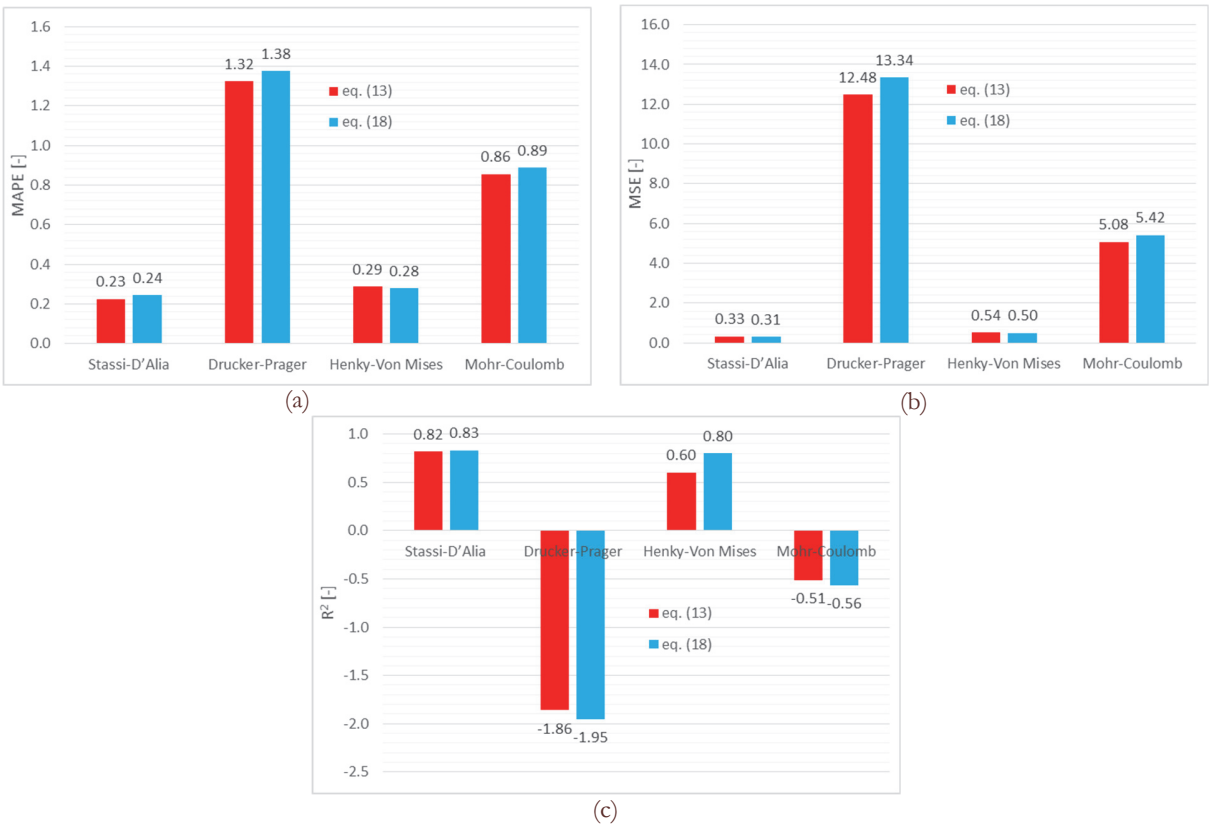

Figure 9: Statistical parameters changing the calculation approach of the effective confining stress, $f_{l,eff}$: a) MAPE, b) MSE and c) R^2.

CONCLUSIONS

Four confinement models were derived by the classical failure criterions available in the scientific literature. These models were used to assess the axial capacity of masonry specimens made of solid clay brick and strengthened with several types of strengthening systems (GFRP, CFRP and BFRP). They were carried out to assess the increase of the axial capacity due to the wrapping interventions. These models are fully based on mechanical parameters representative of the materials: tensile and compressive strengths of masonry and the effective confining stress. The reliability of the mechanical models was assessed by comparison with relevant experimental programs. The strength values are derived by 67 experimental test results. They allow to apply the mechanical model to the masonry specimens actually tested. The effect of confinement is strongly related to the effective confining stress. It was evaluated according to two main approaches available in the literature. Between the several mechanical models the Stassi D'Alia was proposed to assess the axial capacity of confined masonry columns. The reliability of this model was demonstrated by comparing the theoretical values with the experimental results. In order to confirm the potential of this model, the comparison was carried out considering also the other mechanical models. The comparison confirmed the Stassi-D'Alia model to be the best approach to assess the axial capacity of masonry columns made of solid clay brick and strengthened with innovative composite systems. It was remarked both by direct comparison of experimental results with the numerical previsions and by statistical parameters. In particular, the Stassi-D'Alia model provided good fitting for the entire range of the effective confining stresses. The model indicates that the axial capacity of the strengthened masonry is not much influenced by the tensile strength of masonry, despite the model is potentially able to account for such variations if more refined values are

known. The weak influence of the tensile strength of masonry on the axial capacity of the strengthened masonry element is clear, by the experimental results also. It is due to the prevailing confinement effect if compared to that of tensile strength of masonry. The Drucker-Prager model strongly overestimates the experimental results. This effect is very clear for high values of the confining stress, while, for low confining stresses, the mechanical model provides reliable results. However, a great number of tests were carried out at high confining stress values. Therefore, on the entire experimental sample the model provides a weak estimation of the axial capacity of masonry columns wrapped with composites. Furthermore, it results strongly influenced by the tensile strength of masonry providing confinement curves strongly different to change the tensile strength of masonry. The Henchy-Von Mises model does not depend on the normalized tensile strength of confined material. The theoretical and experimental comparison showed a strong underestimation of the experimental values. This effect is clear for the entire confining stress field. The Mohr-Coulomb provides a clear overestimation of the experimental results for the entire experimental sample. In fact, also for low values of the effective confining stress the experimental results are not well fitted by the theoretical results. Furthermore, Mohr-Coulomb results are strongly influenced by the tensile strength of masonry. Finally, the reliability of the Stassi-D'Alia model was remarked by the best values of three statistical parameters: mean absolute percentage error (MAPE), mean square error (MSE) and coefficient of determination (R^2).

REFERENCES

[1] Ramaglia, G., Fabbrocino, F., Lignola, G.P., Prota, A. (2019). Unified theory for flexural strengthening of masonry with composites, Materials (Basel), 12(4). DOI: 10.3390/ma12040680.

[2] Penna, A. (2015). Seismic assessment of existing and strengthened stone-masonry buildings: Critical issues and possible strategies, Bull. Earthq. Eng., 13(4), pp. 1051-1071. DOI: 10.1007/s10518-014-9659-0.

[3] Kwiecień, A., de Felice, G., Oliveira, D. V., Zając, B., Bellini, A., De Santis, S., Ghiassi, B., Lignola, G.P., Lourenço, P.B., Mazzotti, C., Prota, A. (2016). Repair of composite-to-masonry bond using flexible matrix, Mater. Struct. Constr., 48(7), pp. 2563-2580. DOI: 10.1617/s11527-015-0668-5.

[4] Parisi, F., Lignola, G.P., Augenti, N., Prota, A., Manfredi, G. (2013). Rocking response assessment of in-plane laterally-loaded masonry walls with openings, Eng. Struct., 56, pp. 1234-1248. DOI: 10.1016/j.engstruct.2013.06.041.

[5] Ramaglia, G., Lignola, G.P., Fabbrocino, F., Prota, A. (2017). Numerical Modelling of Masonry Barrel Vaults Reinforced with Textile Reinforced Mortars, Key Eng. Mater., 747, pp. 11-19. DOI: 10.4028/www.scientific.net/kem.747.11.

[6] Belliazzi, S., Lignola, G.P., Prota, A. (2018). Textile reinforced mortars systems: a sustainable way to retrofit structural masonry walls under tsunami loads, Int. J. Mason. Res. Innov., 3(3). DOI: 10.1504/ijmri.2018.093484.

[7] Fabbrocino, F., Ramaglia, G., Lignola, G.P., Prota, A. (2019). Ductility-based incremental analysis of curved masonry structures, Eng. Fail. Anal., 97, pp. 653-675. DOI: 10.1016/j.engfailanal.2019.01.027.

[8] Schueremans, L., Cizer, Ö., Janssens, E., Serré, G., Balen, K. Van. (2011). Characterization of repair mortars for the assessment of their compatibility in restoration projects: Research and practice, Constr. Build. Mater., 25(12), pp. 4338-4350. DOI: 10.1016/j.conbuildmat.2011.01.008.

[9] D'Ambrisi, A., Feo, L., Focacci, F. (2013). Experimental and analytical investigation on bond between Carbon-FRCM materials and masonry, Compos. Part B Eng., 45, pp. 15-20. DOI: 10.1016/j.compositesb.2012.10.018.

[10] De Felice, G., Aiello, M.A., Bellini, A., Ceroni, F., De Santis, S., Garbin, E., Leone, M., Lignola, G.P., Malena, M., Mazzotti, C., Panizza, M., Valluzzi, M.R. (2016). Experimental characterization of composite-to-brick masonry shear bond, Mater. Struct. Constr. DOI: 10.1617/s11527-015-0669-4.

[11] Ramaglia, G., Lignola, G.P., Prota, A. (2016). Collapse analysis of slender masonry barrel vaults, Eng. Struct., 117, pp. 86-100. DOI: 10.1016/j.engstruct.2016.03.016.

[12] Giamundo, V., Lignola, G.P., Maddaloni, G., da Porto, F., Prota, A., Manfredi, G. (2016). Shaking table tests on a full-scale unreinforced and IMG retrofitted clay brick masonry barrel vault, Bull. Earthq. Eng., 14(6), pp. 1663-1693. DOI: 10.1007/s10518-016-9886-7.

[13] Marques, R., Lourenço, P.B. (2014). Unreinforced and confined masonry buildings in seismic regions: Validation of macro-element models and cost analysis, Eng. Struct., 65, pp. 52-67. DOI: 10.1016/j.engstruct.2014.01.014.

[14] Okail, H., Abdelrahman, A., Abdelkhalik, A., Metwaly, M. (2016). Experimental and analytical investigation of the lateral load response of confined masonry walls, HBRC J., 12(1), pp. 33-46. DOI: 10.1016/j.hbrcj.2014.09.004.

[15] Ramaglia, G., Russo Spena, F., Lignola, G.P., Prota, A. (2019). Two Parameters Confinement Model for Clay Brick Masonry, Int. J. Comput. Methods. 16(4). DOI: 10.1142/s0219876219400103.

[16] Lignola, G.P., Angiuli, R., Prota, A., Aiello, M.A. (2014). FRP confinement of masonry: analytical modeling, Mater. Struct. Constr., 47(12), pp. 2101-2115. DOI: 10.1617/s11527-014-0323-6.
[17] Lignola, G.P., Nardone, F., Prota, A., Manfredi, G. (2012). Analytical model for the effective strain in FRP-wrapped circular RC columns, Compos. Part B Eng., 43(8). Pp. 523-532. DOI: 10.1016/j.compositesb.2012.04.007.
[18] Lignola, G.P., Prota, A., Manfredi, G., Cosenza, E. (2008). Unified theory for confinement of RC solid and hollow circular columns, Compos. Part B Eng., 39(7-8), pp. 1151-1160. DOI: 10.1016/j.compositesb.2008.03.007.
[19] Stassi-D'Alia, F. (1967). Flow and fracture of materials according to a new limiting condition of yelding, Meccanica, 2(3), pp. 178-195. DOI: 10.1007/bf02128173.
[20] Stassi-D'Alia, F. (1969). Limiting conditions of yielding for anisotropic materials, Meccanica, 4(4), pp. 349-363. DOI: 10.1007/bf02133100.
[21] Popov, E.P. (1999), University of California, Berkley. Engineering Mechanics of Solids (2nd edition).
[22] Meshii, T., Ito, Y. (2012). Proposal of failure criterion applicable to finite element analysis results for wall-thinned pipes under bending load, Nucl. Eng. Des., 242, pp. 34-42. DOI: 10.1016/j.nucengdes.2011.09.032.
[23] Khechai, A., Tati, A., Guettala, A. (2014). Finite element analysis of stress concentrations and failure criteria in composite plates with circular holes, Front. Mech. Eng., 9(3), pp. 291-294. DOI: 10.1007/s11465-014-0307-9.
[24] Noor-E-Khuda S., Albermani F. (2019). Mechanical properties of clay masonry units: Destructive and ultrasonic testing, Constr. Build. Mater., 219, pp. 111-120. DOI: 10.1016/j.conbuildmat.2019.05.166.
[25] Schubert, P. (1994). Tensile and flexural strength of masonry: Influences, test methods, 21 test results. 10th Int. Brick and Block Masonry Conf., Calgary, Canada, 05–07 July, 22 1994.
[26] Drucker, D.C., Prager, W. (1952). Soil mechanics and plastic analysis or limit design, Q. Appl. Math. DOI: 10.1090/qam/48291.
[27] Hill, R. (1948). A theory of the yielding and plastic flow of anisotropic metals, Proc. R. Soc. London. Ser. A. Math. Phys. Sci., 193(1033). DOI: 10.1098/rspa.1948.0045.
[28] Zhang, Z.F., Eckert, J. (2005). Unified tensile fracture criterion, Phys. Rev. Lett., 94(9). DOI: 10.1103/PhysRevLett.94.094301.
[29] Labuz, J.F., Zang, A. (2012). Mohr–Coulomb Failure Criterion, Rock Mech. Rock Eng., 45(6), pp. 975-979. DOI: 10.1007/s00603-012-0281-7.
[30] Handin, J. (1969). On the Coulomb-Mohr failure criterion, J. Geophys. Res. DOI: 10.1029/jb074i022p05343.
[31] CNR-DT 200 R1/2013. (2013). Guide for the design and construction of externally bonded FRP systems for strengthening existing structures, Ital. Natl. Res. Counc.
[32] Krevaikas, T.D., Triantafillou, T.C. (2005). Masonry Confinement with Fiber-Reinforced Polymers, J. Compos. Constr., 9(2). DOI: 10.1061/(asce)1090-0268(2005)9:2(128).
[33] Faella, C., Martinelli, E., Paciello, S., Camorani, G., Aiello, M.A., Micelli, F., Nigro, E. (2011). Masonry columns confined by composite materials: Experimental investigation, Compos. Part B Eng., 42(4), pp. 692-704. DOI: 10.1016/j.compositesb.2011.02.001.
[34] Di Ludovico, M., D'Ambra, C., Prota, A., Manfredi, G. (2010). FRP Confinement of Tuff and Clay Brick Columns: Experimental Study and Assessment of Analytical Models, J. Compos. Constr., 14(5). DOI: 10.1061/(asce)cc.1943-5614.0000113.
[35] Alecci, V., Briccoli Bati, S., Ranocchiai, G. (2009). Study of Brick Masonry Columns Confined with CFRP Composite, J. Compos. Constr., 13(3). DOI: 10.1061/(asce)1090-0268(2009)13:3(179).
[36] Bieker, C., Seim, W., and Stürz, J. (2002). Post-strengthening of masonry columns by use of fiber-reinforced polymers. Proc., ICCI'02-3rd Int. Conf. of Composites in Infrastructure, San Francisco.
[37] Rao, K.S.N., Pavan, G.S. (2014). FRP-Confined Clay Brick Masonry Assemblages under Axial Compression: Experimental and Analytical Investigations, J. Compos. Constr., 19(4). DOI: 10.1061/(asce)cc.1943-5614.0000525.
[38] Corradi, M., Grazini, A., Borri, A. (2007). Confinement of brick masonry columns with CFRP materials, Compos. Sci. Technol., 67, 1772-1783. DOI: 10.1016/j.compscitech.2006.11.002.
[39] Krevaikas, T.D., Triantafillou, T.C. (2005). Masonry Confinement with Fiber-Reinforced Polymers, J. Compos. Constr. DOI: 10.1061/(asce)1090-0268(2005)9:2(128).
[40] Aiello, M.A., Micelli, F., Valente, L. (2009). FRP Confinement of Square Masonry Columns, J. Compos. Constr., 13(2). DOI: 10.1061/(asce)1090-0268(2009)13:2(148).
[41] ASTM E519M-15 (2015) Standard Test Method for Diagonal Tension (Shear) in Masonry 23 Assemblages, ASTM International, West Conshohocken, PA.

APPENDIX A

Mechanical properties of constituents in terms of compressive strength, f, tensile strength, f_t, tensile strain, ε_t and Young's modulus, E. These parameters refer to the experimental programs used for theoretical and numerical comparison.

Element	f [MPa]	f_t [MPa]	ε_t [-]	E [GPa]
Mortar	1.03	-	-	-
Epoxy resin (type a)	30	30	-	3
Epoxy resin (type b)	25	25	-	3.1
GFRP (type a)	2560	-	0.032	80.7
GFRP (type b)	1600	-	0.025	65

Table 1.A: Mechanical properties of constituents for the experimental tests [33].

Element	f [MPa]	f_t [MPa]	ε_t [-]	E [GPa]
Mortar	6.9	1.71	-	-
Brick	22.71	-	-	-
Epoxy resin	-	40	0.0018	3
BFRP	-	1814	0.019	91
GFRP	-	1371	0.021	69

Table 2.A: Mechanical properties of constituents for the experimental tests [34].

Element	f [MPa]	f_t [MPa]	E [MPa]
Mortar	2.1	-	577
Brick	15.7	-	3058
Unconfined masonry	13.6	-	-
Resin	-	50	3000
Carbon	-	3430	230000

Table 3.A: Mechanical properties of constituents for the experimental tests [35].

Element	f [MPa]	f_t [MPa]	ε_t [-]	E [GPa]
Solid clay brick	20	-	-	-
Hollow clay brick	12	-	-	-
Calcium mortar (type a)	1	-	-	-
Cementitious mortar (type b)	5.1	-	-	-
Epoxy resin	-	30	-	3.8
CFRP	-	3500	0.015	230
GFRP	-	2250	0.031	70

Table 4.A: Mechanical properties of constituents for the experimental tests [36].

Element	f [MPa]	f_t [MPa]	ε_t [-]	E [GPa]
Clay brick	7.65	-	0.0064	1.96
Cement mortar	7.0	-	0.0018	11.2
CFRP-Gr200	-	230	0.015	25.1
GFRP-Gr200	-	110	0.031	10.6
GFRP-Gr360	-	175	0.031	11.6

Table 5.A: Mechanical properties of constituents for the experimental tests [37].

Element	f [MPa]	f_t [MPa]	ε_t [-]	E [GPa]
Clay brick, series 1	20.78	-	-	-
Clay brick, series 2	27.45	-	-	-
Cement mortar	10	3.36	-	-
CFRP-HT	-	3338	0.00799	417.6
CFRP-VHM	-	1955	0.00307	637.2

Table 6.A: Mechanical properties of constituents for the experimental tests [38].

Element	f [MPa]	f_t [MPa]	ε_t [-]	E [GPa]
Brick	23.5	-	-	-
Mortar	2.23	-	-	-
CFRP	-	3500	0.015	230
GFRP	-	2000	0.029	70

Table 7.A: Mechanical properties of constituents for the experimental tests [39].

Element	f [MPa]	f_t [MPa]	ε_t [-]	E [GPa]
Brick	23.5	-	-	-
Mortar	2.23	-	-	-
CFRP	-	3500	0.015	230
GFRP	-	2000	0.029	70

Table 8.A: Mechanical properties of constituents for the experimental tests [40].

APPENDIX B

Geometrical characteristics of the specimens (cross-section, b×d and height, h), type of fiber, number of layers, n_l, equivalent thickness, t_{eq}, unconfined compressive strength, f_{m0} and confined compressive strength, f_{mc}, normalized confined compressive strength, f_{mc} / f_{m0}, effective confining stress, $f_{l,eff}$, normalized effective confining stress, $f_{l,eff} / f_{m0}$ calculated according to Eqns. (13) and (18).

ID specimen	b [mm]	d [mm]	h [mm]	Type of fiber [-]	n_l [-]	t_{eq} [mm]	f_{mc} [MPa]	f_{m0} [MPa]	f_{mc}/f_{mc0} [-]
S1	250	250	500	GFRP (type a)	1	0.48	19.29	13.71	1.407
S2	250	250	250	GFRP (type a)	1	0.48	26.23	13.98	1.876
S3	250	250	250	GFRP (type a)	1	0.48	21.21	13.98	1.518
S4	250	250	250	GFRP (type a)	2	0.96	35.18	13.98	2.517
S5	250	250	250	GFRP (type a)	2	0.96	30.52	13.98	2.184
S6	380	383	492	GFRP (type b)	1	0.23	12.03	8.3	1.426
S7	387	375	485	GFRP (type b)	1	0.23	12.79	8.3	1.518
S8	377	380	488	GFRP (type b)	1	0.23	14.15	8.3	1.678
S9	383	378	486	GFRP (type b)	2	0.46	14.52	8.43	1.723
S10	377	378	481	GFRP (type b)	2	0.46	16.01	8.43	1.899
S11	383	374	492	GFRP (type b)	2	0.46	12.64	8.43	1.499
S12	250	248	470	GFRP (type b)	1	0.23	17.65	11.12	1.588
S13	250	249	470	GFRP (type b)	1	0.23	16.27	11.12	1.463
S14	250	247	470	GFRP (type b)	1	0.23	15.94	11.12	1.434
S15	248	247	462	GFRP (type b)	2	0.46	19.10	11.12	1.718
S16	245	248	471	GFRP (type b)	2	0.46	20.57	11.12	1.850
S17	246	251	473	GFRP (type b)	2	0.46	21.45	11.12	1.929

Table 1.B: Geometrical characteristics and experimental results [33].

ID specimen	k_{eff} [-]	$f_{l,(eq.13)}$ [MPa]	$f_{l,eff,(eq.13)}$ [MPa]	$(f_{l,eff}/ f_{m0})$, (eq.13) [MPa]	$f_{l,(eq.18)}$ [MPa]	$f_{l,eff,(eq.18)}$ [MPa]	$(f_{l,eff}/ f_{m0})$, (eq.18) [MPa]
S1	0.38	9.830	3.782	0.276	9.830	3.782	0.276
S2	0.38	9.830	3.782	0.271	9.830	3.782	0.271
S3	0.38	9.830	3.782	0.271	9.830	3.782	0.271
S4	0.38	19.661	7.565	0.541	19.661	7.565	0.541
S5	0.38	19.661	7.565	0.541	19.661	7.565	0.541
S6	0.42	1.922	0.799	0.095	1.929	0.802	0.095
S7	0.42	1.902	0.790	0.094	1.932	0.803	0.095
S8	0.42	1.937	0.806	0.096	1.945	0.809	0.096
S9	0.42	3.843	1.598	0.190	3.869	1.609	0.191
S10	0.42	3.894	1.622	0.192	3.899	1.624	0.193
S11	0.42	3.843	1.599	0.190	3.890	1.619	0.192
S12	0.46	2.944	1.342	0.121	2.956	1.347	0.121
S13	0.46	2.944	1.341	0.121	2.950	1.344	0.121
S14	0.46	2.944	1.342	0.121	2.962	1.350	0.121
S15	0.46	5.935	2.709	0.244	5.947	2.715	0.244
S16	0.46	5.935	2.712	0.244	5.972	2.728	0.245
S17	0.46	5.865	2.673	0.240	5.924	2.701	0.243

Table 2.B: Effective confining stress calculated according to Eqns. (13) and (18) for the experimental program, [33].

ID specimen	b [mm]	d [mm]	h [mm]	Type of fiber [-]	n_l [-]	t_{eq} [mm]	f_{mc} [MPa]	f_{m0} [MPa]	f_{mc}/f_{mc0} [-]
S18	264	265	560	Glass	1	0.48	9.97	6.22	1.604
S19	267	265	560	Glass	1	0.48	8.53	6.22	1.372
S20	266	265	560	Glass	1	0.48	11.29	6.22	1.817
S21	266	266	560	Basalt	1	0.24	10.40	6.22	1.673
S22	265	264	560	Basalt	1	0.24	9.82	6.22	1.580
S23	265	264	560	Basalt	1	0.24	10.20	6.22	1.640

Table 3.B: Geometrical characteristics and experimental results [34].

ID specimen	k_{eff} [-]	$f_{l,(eq.13)}$ [MPa]	$f_{l,eff,(eq.13)}$ [MPa]	$(f_{l,eff}/ f_{m0})$, (eq.13) [MPa]	$f_{l,(eq.18)}$ [MPa]	$f_{l,eff,(eq.18)}$ [MPa]	$(f_{l,eff}/ f_{m0})$, (eq.18) [MPa]
S18	2.48	5.80	2.48	0.399	5.81	2.48	0.399
S19	2.46	5.75	2.46	0.395	5.77	2.47	0.397
S20	2.47	5.77	2.47	0.397	5.79	2.47	0.398
S21	1.40	3.27	1.40	0.225	3.27	1.40	0.225
S22	1.40	3.29	1.40	0.226	3.29	1.41	0.226
S23	1.40	3.29	1.40	0.226	3.29	1.41	0.226

Table 4.B: Effective confining stress calculated according to Eqns. (13) and (18) for the experimental program, [34].

ID specimen	b [mm]	d [mm]	h [mm]	Type of fiber [-]	n_l [-]	t_{eq} [mm]	f_{mc} [MPa]	f_{m0} [MPa]	f_{mc}/f_{mc0} [-]
S24	54	54	85	Carbon	0.125	0.0206	20.63	13.58	1.519
S25	54	54	85	Carbon	0.25	0.0413	27.38	13.58	2.016
S26	54	54	85	Carbon	0.167	0.0275	22.80	13.58	1.679

Table 5.B: Geometrical characteristics and experimental results [35].

ID specimen	k_{eff} [-]	$f_{l,(eq.13)}$ [MPa]	$f_{l,eff,(eq.13)}$ [MPa]	$(f_{l,eff}/ f_{m0})$, (eq.13) [MPa]	$f_{l,(eq.18)}$ [MPa]	$f_{l,eff,(eq.18)}$ [MPa]	$(f_{l,eff}/ f_{m0})$, (eq.18) [MPa]
S24	0.15	2.62	0.40	0.0292	2.62	0.40	0.0292
S25	0.15	5.24	0.79	0.0583	5.24	0.79	0.0583
S26	0.15	3.49	0.53	0.0389	3.49	0.53	0.0389

Table 6.B: Effective confining stress calculated according to Eqns. (13) and (18) for the experimental program [35].

ID specimen	b [mm]	d [mm]	h [mm]	Type of fiber [-]	n_l [-]	t_{eq} [mm]	f_{mc} [MPa]	f_{m0} [MPa]	f_{mc}/f_{mc0} [-]
S27	240	240	500	Carbon	1	0.131	13.374	5.295	2.526
S28	240	240	500	Carbon	2	0.262	14.922	5.295	2.818
S29	240	240	500	Glass	2	0.34	12.142	5.295	2.293
S30	240	240	500	Glass	3	0.51	13.215	5.295	2.496
S31	240	240	500	Carbon	1	0.131	4.751	3.299	1.440
S32	240	240	500	Carbon	2	0.262	5.279	3.299	1.600
S33	240	240	500	Glass	2	0.34	5.930	3.299	1.798
S34	240	240	500	Glass	3	0.51	5.948	3.299	1.803

Table 7.B: Geometrical characteristics and experimental results [36].

ID specimen	k_{eff} [-]	$f_{l,(eq.13)}$ [MPa]	$f_{l,eff,(eq.13)}$ [MPa]	$(f_{l,eff}/ f_{m0})$, (eq.13) [MPa]	$f_{l,(eq.18)}$ [MPa]	$f_{l,eff,(eq.18)}$ [MPa]	$(f_{l,eff}/ f_{m0})$, (eq.18) [MPa]
S27	0.48	3.77	1.82	0.343	3.77	1.82	0.343
S28	0.48	7.53	3.64	0.687	7.53	3.64	0.687
S29	0.48	6.15	2.97	0.560	6.15	2.97	0.560
S30	0.48	9.22	4.45	0.841	9.22	4.45	0.841
S31	0.48	3.77	1.82	0.551	3.77	1.82	0.551
S32	0.48	7.53	3.64	1.102	7.53	3.64	1.102
S33	0.48	6.15	2.97	0.900	6.15	2.97	0.900
S34	0.48	9.22	4.45	1.349	9.22	4.45	1.349

Table 8.B: Effective confining stress calculated according to Eqns. (13) and (18) for the experimental program [36].

ID specimen	b [mm]	d [mm]	h [mm]	Type of fiber [-]	n_l [-]	t_{eq} [mm]	f_{mc} [MPa]	f_{m0} [MPa]	f_{mc}/f_{mc0} [-]
S35	225	105	415	Glass	1	0.467	8.08	5.60	1.443
S36	225	105	415	Glass	1	0.242	8.02	5.60	1.432
S37	225	105	415	Glass	1	0.274	6.95	5.60	1.241
S38	225	105	415	Carbon	1	0.371	6.61	5.60	1.180
S39	150	105	320	Glass	1	0.369	7.27	3.68	1.976
S40	150	105	300	Glass	1	0.370	5.95	1.78	3.343
S41	150	105	300	Glass	1	0.223	4.80	1.54	3.117
S42	245	105	460	Glass	1	0.347	9.19	6.15	1.494
S43	245	105	460	Glass	1	0.200	9.75	6.15	1.585
S44	245	105	460	Carbon	1	0.412	8.14	6.15	1.324
S45	225	222	420	Glass	1	0.316	7.73	4.62	1.673
S46	225	222	420	Glass	1	0.443	7.50	4.62	1.623
S47	225	249	460	Glass	1	0.675	8.26	4.32	1.912
S48	225	249	460	Glass	1	0.467	8.00	4.32	1.852

Table 9.B: Geometrical characteristics and experimental results [37].

ID specimen	k_{eff} [-]	$f_{l,(eq.13)}$ [MPa]	$f_{l,eff,(eq.13)}$ [MPa]	$(f_{l,eff}/ f_{m0})$, (eq.13) [MPa]	$f_{l,(eq.18)}$ [MPa]	$f_{l,eff,(eq.18)}$ [MPa]	$(f_{l,eff}/ f_{m0})$, (eq.18) [MPa]
S35	0.29	0.47	0.14	0.025	0.73	0.22	0.039
S36	0.29	1.31	0.39	0.069	2.06	0.61	0.108
S37	0.29	0.24	0.07	0.012	0.37	0.11	0.020
S38	0.29	0.56	0.17	0.030	0.88	0.26	0.046
S39	0.48	0.86	0.41	0.112	1.05	0.50	0.136
S40	0.48	0.86	0.41	0.231	1.05	0.50	0.281
S41	0.48	0.86	0.41	0.268	1.05	0.50	0.326
S42	0.24	0.32	0.08	0.012	0.53	0.13	0.021
S43	0.24	0.89	0.21	0.035	1.49	0.36	0.058
S44	0.24	0.38	0.09	0.015	0.63	0.15	0.024
S45	0.44	0.64	0.28	0.062	0.65	0.29	0.062
S46	0.44	0.89	0.39	0.085	0.89	0.40	0.086
S47	0.43	0.62	0.27	0.063	0.66	0.29	0.066
S48	0.43	1.71	0.74	0.172	1.80	0.78	0.181

Table 10.B: Effective confining stress calculated according to Eqn. (13) and (18) for the experimental program, [37].

ID specimen	b [mm]	d [mm]	h [mm]	Type of fiber [-]	n_l [-]	t_{eq} [mm]	f_{mc} [MPa]	f_{m0} [MPa]	f_{mc}/f_{mc0} [-]
S49	245	250	500	Carbon-HT	2	0.330	24.39	14.63	1.667
S50	245	250	500	Carbon-VHM	2	0.286	22.37	14.63	1.529
S51	245	250	500	Carbon-HT	2	0.330	29.99	14.63	2.050
S52	245	250	500	Carbon-VHM	2	0.286	26.84	14.63	1.835

Table 11.B: Geometrical characteristics and experimental results [38].

ID specimen	k_{eff} [-]	$f_{l,(eq.13)}$ [MPa]	$f_{l,eff,(eq.13)}$ [MPa]	$(f_{l,eff}/ f_{m0})$, (eq.13) [MPa]	$f_{l,(eq.18)}$ [MPa]	$f_{l,eff,(eq.18)}$ [MPa]	$(f_{l,eff}/ f_{m0})$, (eq.18) [MPa]
S49	0.33	8.944	0.204	0.204	9.04	3.01	0.206
S50	0.33	4.473	0.102	0.102	4.52	1.51	0.103
S51	0.44	8.944	0.267	0.267	9.04	3.94	0.270
S52	0.44	4.473	0.134	0.134	4.52	1.97	0.135

Table 12.B: Effective confining stress calculated according to Eqn. (13) and (18) for the experimental program, [38].

ID specimen	b [mm]	d [mm]	h [mm]	Type of fiber [-]	n_l [-]	t_{eq} [mm]	f_{mc} [MPa]	f_{m0} [MPa]	f_{mc}/f_{mc0} [-]
S53	115	115	340	Carbon	1	0.117	13.63	12.07	1.129
S54	115	115	340	Carbon	2	0.234	16.92	12.07	1.402
S55	115	115	340	Carbon	3	0.351	25.42	12.07	2.106
S56	115	115	340	Glass	5	0.750	40.00	12.07	3.314
S57	115	115	340	Carbon	1	0.117	16.87	12.07	1.398
S58	115	115	340	Carbon	2	0.234	23.91	12.07	1.981
S59	115	115	340	Carbon	3	0.351	34.69	12.07	2.874
S60	115	115	340	Glass	5	0.750	44.87	12.07	3.717
S61	172.5	115	340	Carbon	2	0.234	11.90	6.65	1.789
S62	172.5	115	340	Carbon	3	0.351	17.29	6.65	2.600
S63	172.5	115	340	Glass	5	0.750	24.37	6.65	3.665
S64	230	115	340	Carbon	2	0.234	11.79	6.21	1.899
S65	230	115	340	Carbon	3	0.351	12.00	6.21	1.932
S66	230	115	340	Glass	5	0.750	17.81	6.21	2.868

Table 13.B: Geometrical characteristics and experimental results [39].

ID specimen	k_{eff} [-]	$f_{l,(eq.13)}$ [MPa]	$f_{l,eff,(eq.13)}$ [MPa]	$(f_{l,eff}/ f_{m0})_{,(eq.13)}$ [MPa]	$f_{l,(eq.18)}$ [MPa]	$f_{l,eff,(eq.18)}$ [MPa]	$(f_{l,eff}/ f_{m0})_{,(eq.18)}$ [MPa]
S53	0.44	7.02	3.09	0.256	7.02	3.09	0.256
S54	0.44	14.24	6.28	0.520	14.24	6.28	0.520
S55	0.44	21.37	9.41	0.780	21.37	9.41	0.780
S56	0.44	26.09	11.49	0.952	26.09	11.49	0.952
S57	0.53	7.12	3.80	0.314	7.12	3.80	0.314
S58	0.53	14.24	7.59	0.629	14.24	7.59	0.629
S59	0.53	21.37	11.39	0.943	21.37	11.39	0.943
S60	0.53	26.09	13.90	1.152	26.09	13.90	1.152
S61	0.37	9.50	3.50	0.526	11.87	4.37	0.657
S62	0.37	14.24	5.25	0.789	17.80	6.56	0.986
S63	0.37	17.39	6.41	0.963	21.74	8.01	1.204
S64	0.25	7.12	1.77	0.285	10.68	2.66	0.428
S65	0.25	10.68	2.66	0.428	16.02	3.98	0.642
S66	0.25	13.04	3.24	0.522	19.57	4.87	0.783

Table 14.B: Effective confining stress calculated according to Eqn. (13) and (18) for the experimental program, [39].

ID specimen	b [mm]	d [mm]	h [mm]	Type of fiber [-]	n_l [-]	t_{eq} [mm]	f_{mc} [MPa]	f_{m0} [MPa]	f_{mc}/f_{mc0} [-]
S67	250	250	500	Glass	1	0.48	19.65	13.72	1.432

Table 15.B: Geometrical characteristics and experimental results [40].

ID specimen	k_{eff} [-]	$f_{l,(eq.13)}$ [MPa]	$f_{l,eff,(eq.13)}$ [MPa]	$(f_{l,eff}/ f_{m0})$, (eq.13) [MPa]	$f_{l,(eq.18)}$ [MPa]	$f_{l,eff,(eq.18)}$ [MPa]	$(f_{l,eff}/ f_{m0})$, (eq.18) [MPa]
S67	0.38	6.16	2.37	0.173	6.16	2.37	0.173

Table 16.B: Effective confining stress calculated according to Eqns. (13) and (18) for the experimental program, [40].